Supplement of Geosci. Model Dev., 11, 4843–4871, 2018
https://doi.org/10.5194/gmd-11-4843-2018-supplement

Geoscientific Model Development
Open Access

Supplement of

A Lagrangian approach towards extracting signals of urban CO_2 emissions from satellite observations of atmospheric column CO_2 (XCO_2): X-Stochastic Time-Inverted Lagrangian Transport model ("X-STILT v1")

Dien Wu et al.

Correspondence to: Dien Wu (dien.wu@utah.edu)

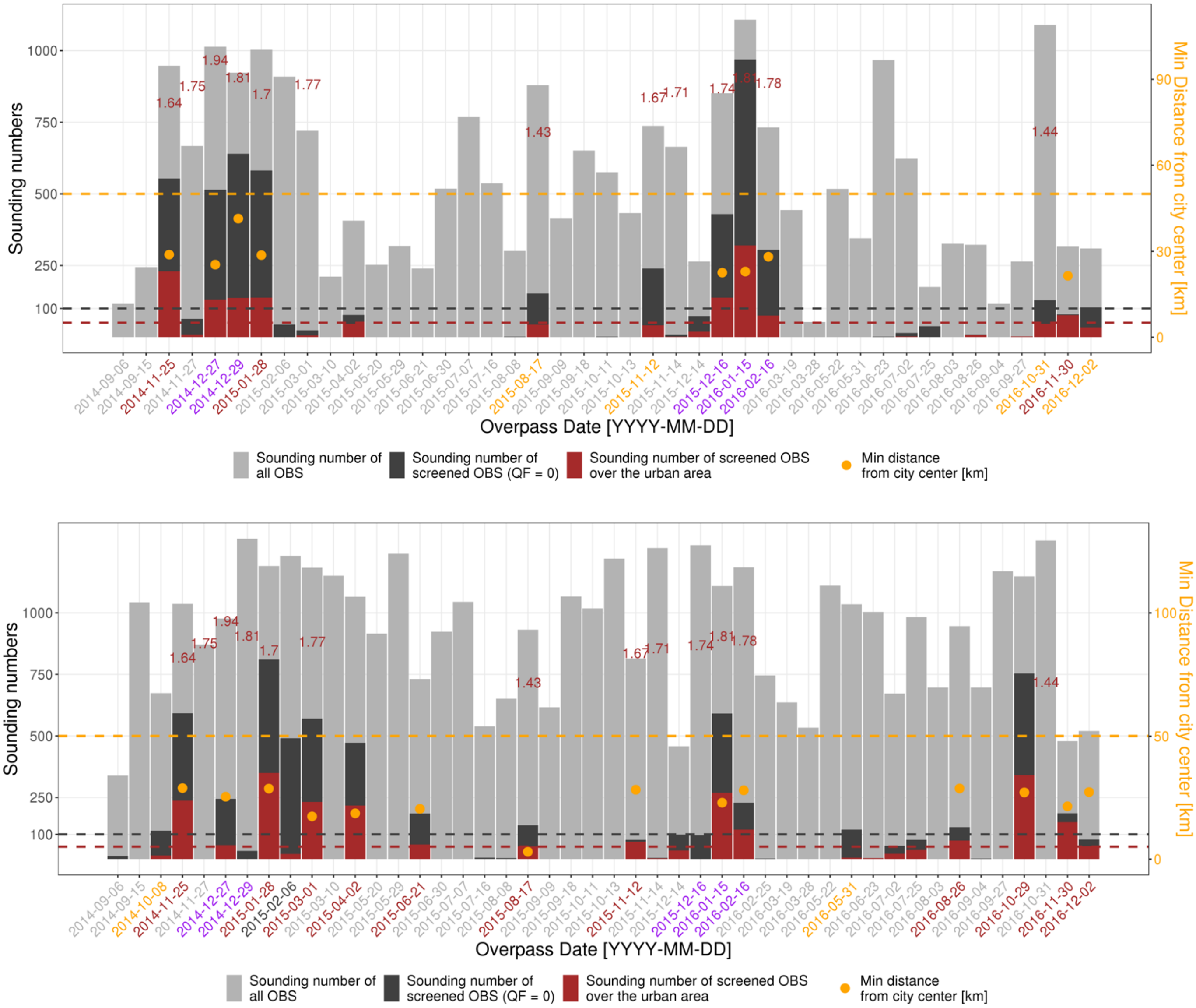

Figure S1. Time series of sounding numbers that fall into a designed spatial domain (3° by 2° box centered around the city) without (grey bars) and with data screening (QF = 0, black bars) per overpass with y-axis to the left, based on observations from b7 (upper panel) or b8 (lower panel) Lite product. Red bars denote the sounding number within a designed urban area (1° by 1° centered around the city). Orange dots indicate the smallest distance (in km) between soundings and the city center (24.71° N, 46.71° E) with orange y-axis to the right. Regional mean u- and v-component GDAS wind errors [m s^{-1}] below 3 km during back-trajectory period are labeled as numbers in brown. These wind RMSE are consistent with those in Table 1. Overpasses are narrowed down using filters of at least 100 screened soundings (black dashed line), falling within the circle of a 50 km radius around the city center (orange dashed line), and relatively smaller regional wind errors (< 2 m s^{-1}, in brown text). We chose to examine 5 overpasses labeled in purple for Riyadh. In general, improvements in b8 algorithms yield slightly more screened observations than b7 over Riyadh from 2014 to 2016.

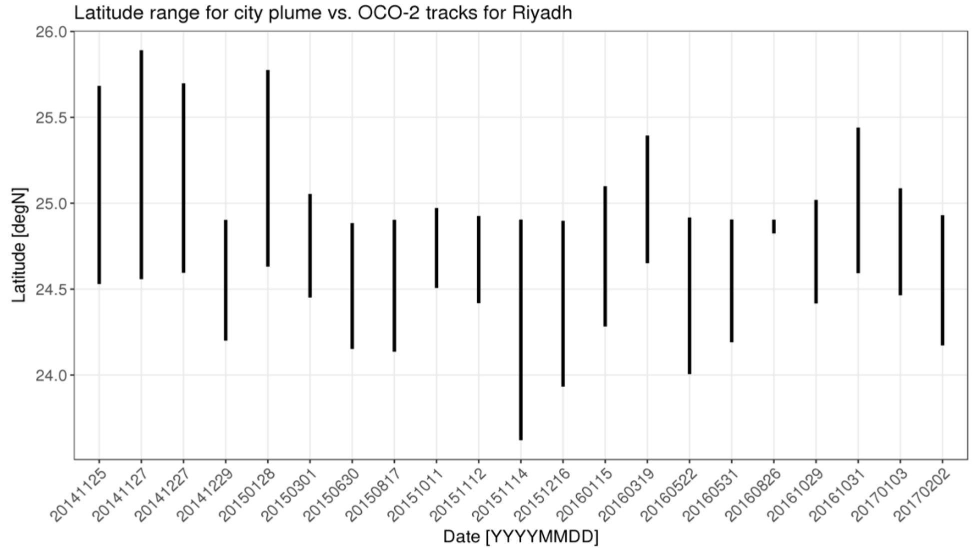

Figure S2. Time series of the latitude range of the city plume derived from the forward-time trajectories, with near-field transport errors included, for several overpasses over Riyadh. The latitude range for overpass date on 20141229 here in this figure is the same as the enhanced latitude range indicated by red triangles in **Fig. 5**. Derivation of these enhanced latitude ranges is described in Sect. 2.3.3.

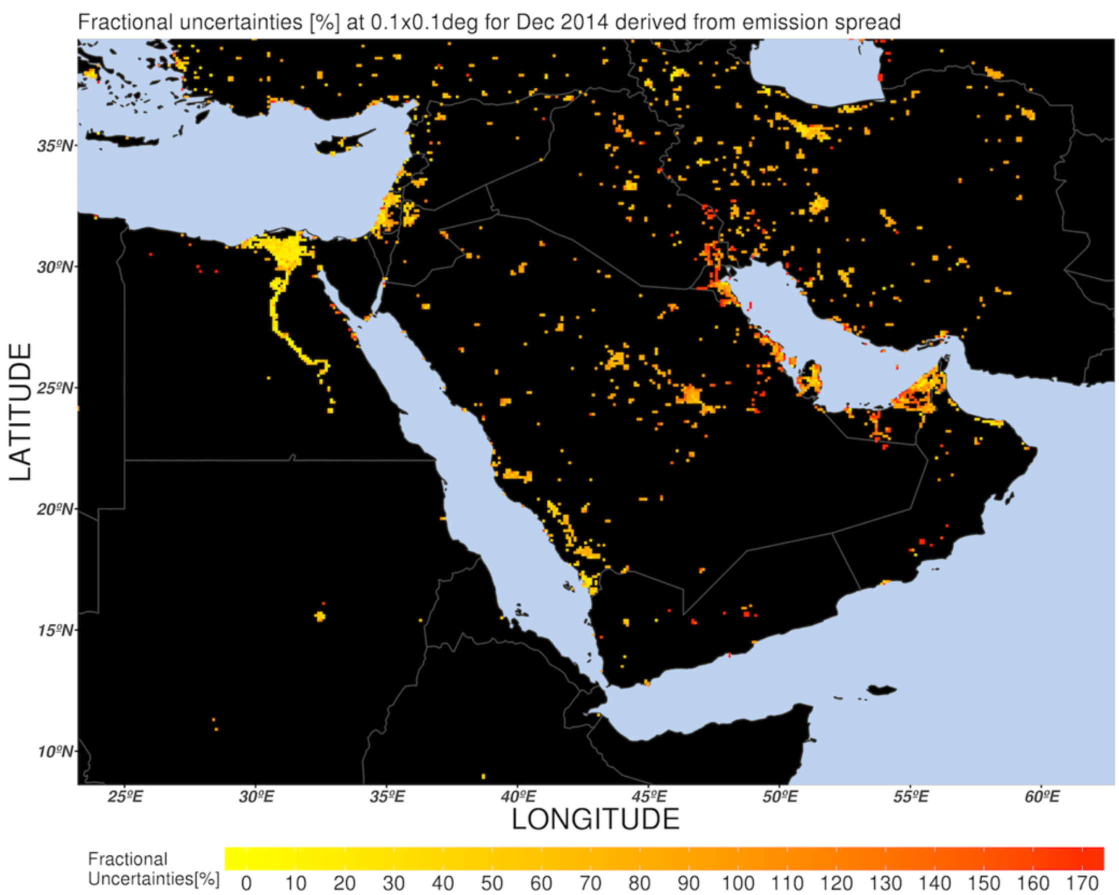

Figure S3. Map of 0.1° × 0.1° fractional uncertainties (%) of FFCO$_2$ emissions derived from the 1-σ among 3 emission inventories (ODIAC, FFDAS and EDGAR). Only fractional uncertainties with large ODIAC emissions (>1 μmole m^{-2} s^{-1}) using this spread method are displayed.

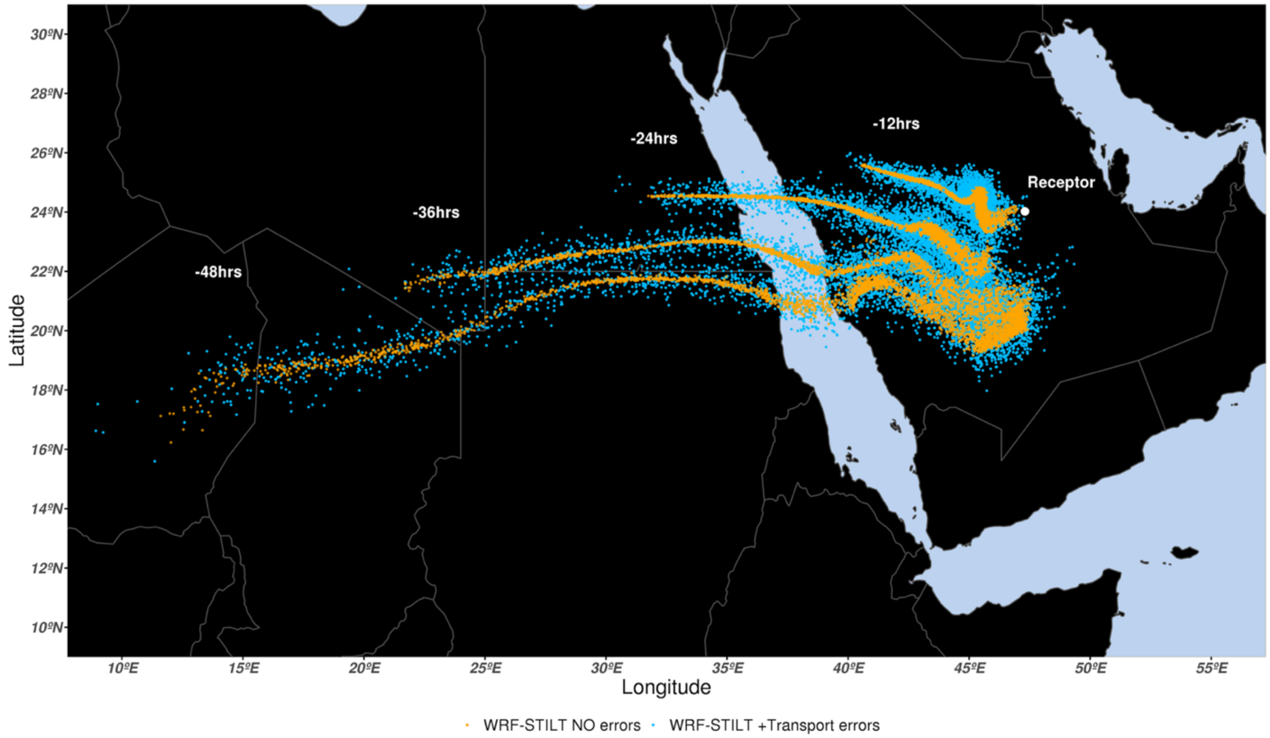

Figure S4. Spatial map of backward particle distributions released from a column receptor, without (orange) and with (blue) regional wind errors (at 12, 24, 36, 48 hours back). Note that only particles released from receptors below 3 km are plotted. For each time step, particles at higher vertical levels locate to the west of those near the surface.

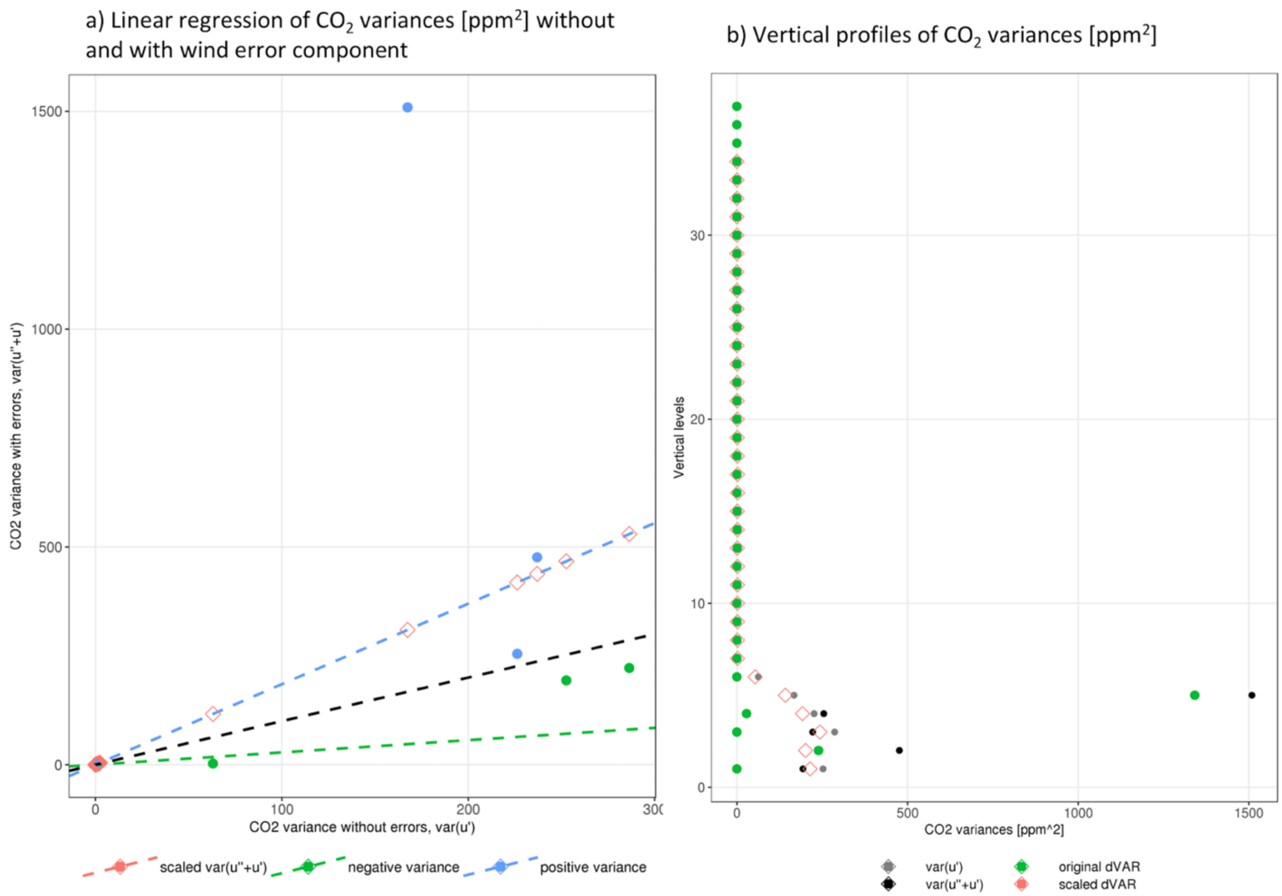

Figure S5. Demostrations of the new regression-based transport error algorithm, to resolve the techinial issue where negative difference in variance occur when parcels are statistically insufficient (green dots). Note that u'' in the figure simple means ε. **a)** Solid dots represent the errors in CO_2 among air parcels without ($\sigma^2_{u'}$) and with wind error component ($\sigma^2_{\varepsilon+u'}$) for each model release level. Linear regression line (green dashed line) is fitted for levels where $\sigma^2_{u'}$ is larger than $\sigma^2_{\varepsilon+u'}$ (green dots). Weighted linear regression line (blue dashed line) is fitted for normal cases where $\sigma^2_{u'}$ is smaller than $\sigma^2_{\varepsilon+u'}$ (blue dots), with weights of $1/\sigma^2_{\varepsilon+u'}$. The weighted regression line descibes the overall increase in CO_2 variances due to the randomization over all X-STILT levels. Then, we recalculate the $\sigma^2_{\varepsilon+u'}$ based on $\sigma^2_{u'}$ and weighted regression line, as scaled $\sigma^2_{\varepsilon+u'}$ (red squares). **b)** Vertical profiles of CO_2 variances without or with the wind error component (grey or black dots), difference between $\sigma^2_{u'}$ and original $\sigma^2_{\varepsilon+u'}$ (green sqaures) and difference between $\sigma^2_{u'}$ and scaled $\sigma^2_{\varepsilon+u'}$ (red squares). If differeces between $\sigma^2_{u'}$ and original $\sigma^2_{\varepsilon+u'}$ are negative for certain lower levels, we assigned them as 0. The final transport error per level is calculated as the difference between $\sigma^2_{u'}$ and scaled $\sigma^2_{\varepsilon+u'}$ (red squares). Note that the notations of var(u'+u'') and var(u') in the plot legend are the same as $\sigma^2_{\varepsilon+u'}$ and $\sigma^2_{u'}$.

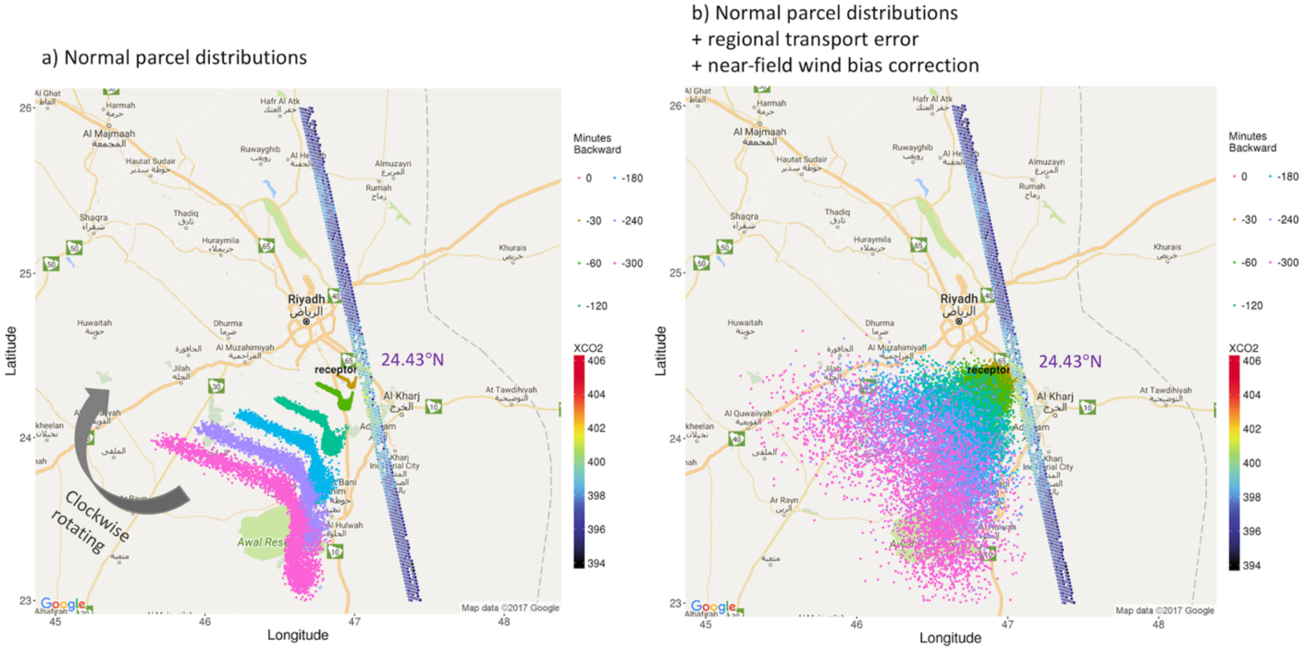

Figure S6. Demonstration of impacts of regional transport errors and near-field wind biases on parcel distributions. Original backward trajectories (**a**) and trajectories with both wind error perturbation and near-field wind corrections (**b**), at 0.5, 1, 2, 3, 4, 5 hours back in time (different colors) released from latitude at ~24.43° N, along with observed XCO_2. In this example, we rotated model trajectories based on prescribed wind biases (e.g., u = +0.3m/s; v = -1.1m/s).

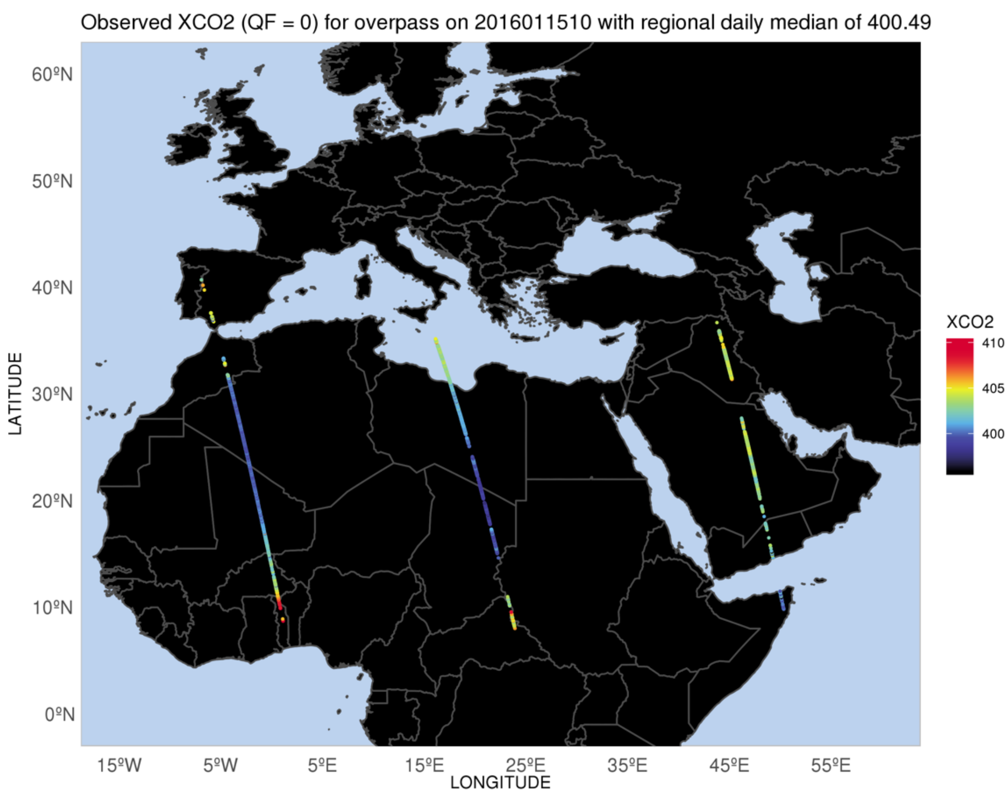

Figure S7. Regional observed XCO_2 on 01/15/2016. Displayed spatial domain is chosen according to the spatial domain used for background estimates in Hakkarainen et al. (2016), which results in the background value of 400.49 ppm. In contrast, the overpass-specific (M3) background is about 402.44 ppm.

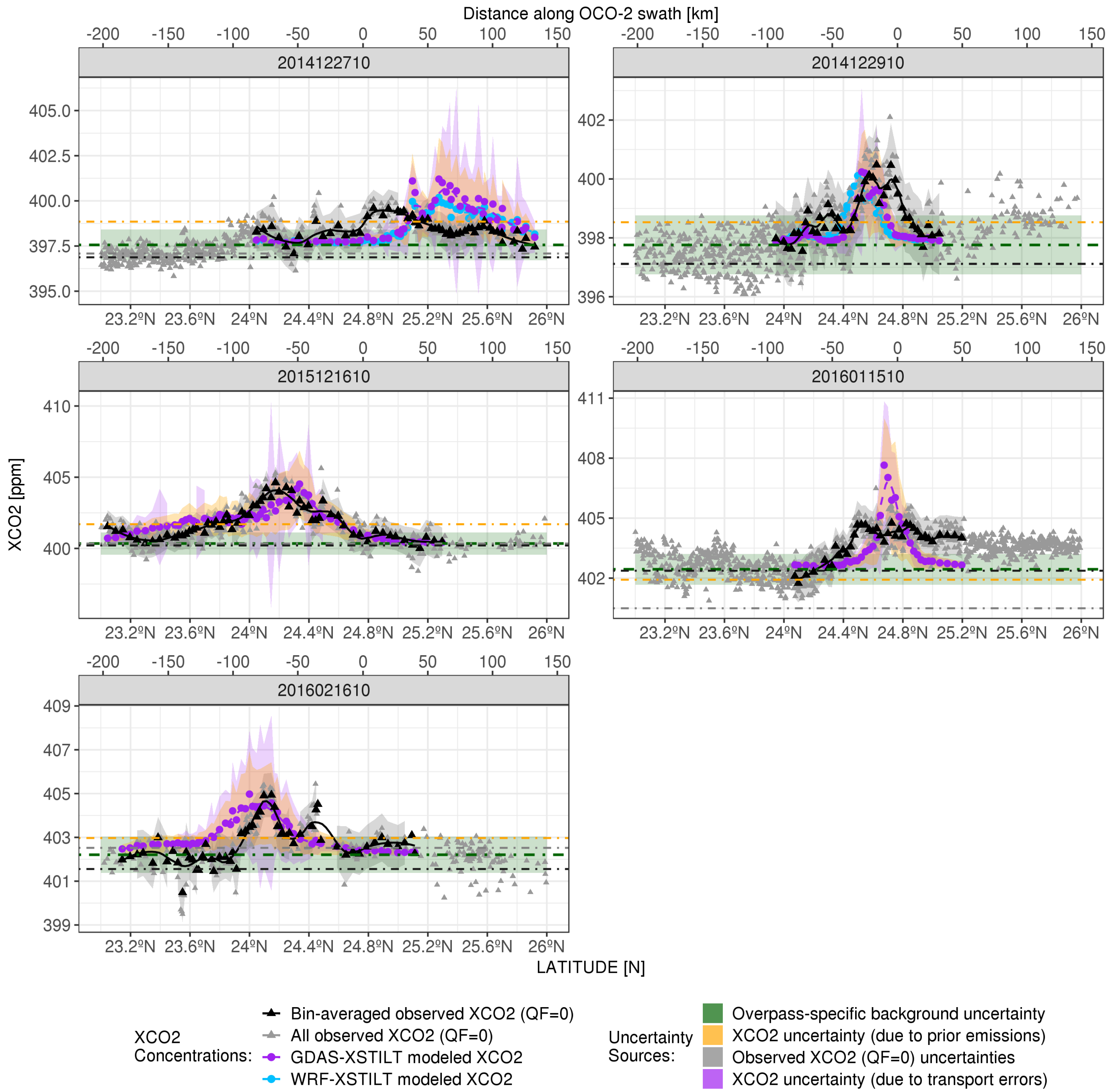

Figure S8. Same as **Fig. 8**, but for all five overpasses examined over Riyadh using OCO-2 Lite v7.

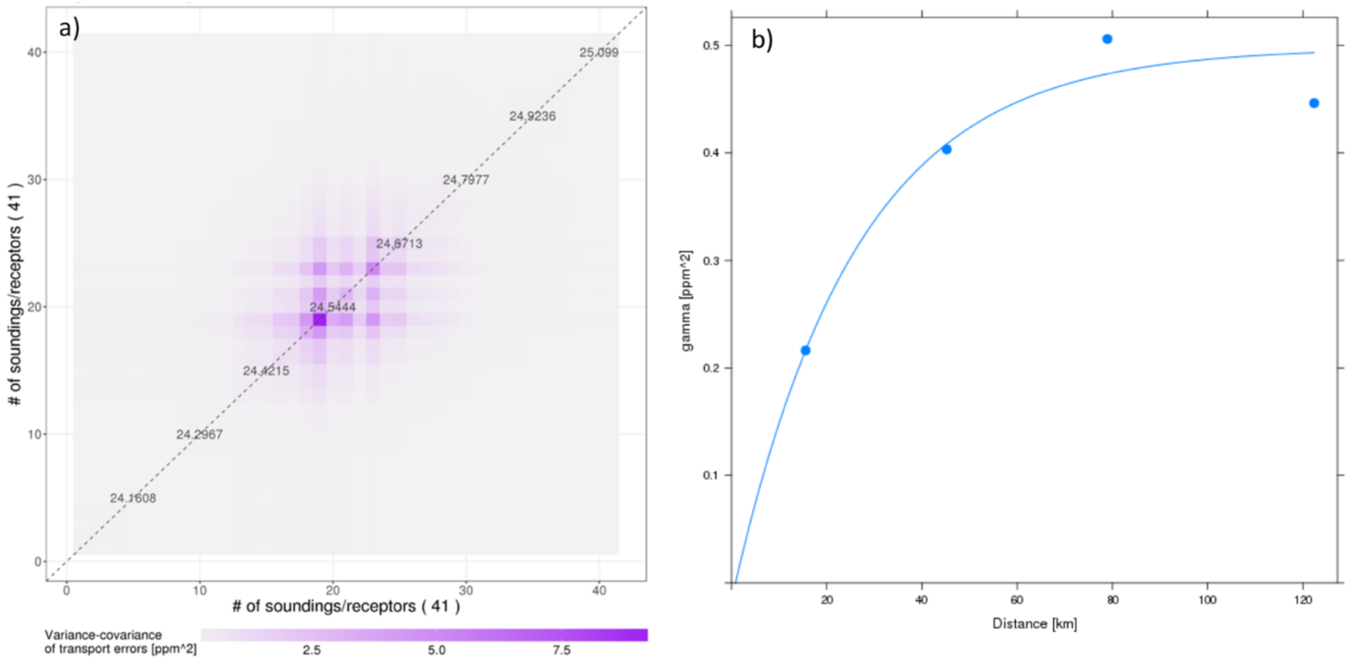

Figure S9. a) An example of transport error covariance matrix with a horizontal correlation lengthscale of 25 km for overpass on 12/29/2014. **b)** Exponential variogram for estimating the horizontal lengthscale (km) of transport errors between each two modeled receptors/sampled soundings, for the overpass on 12/29/2014.

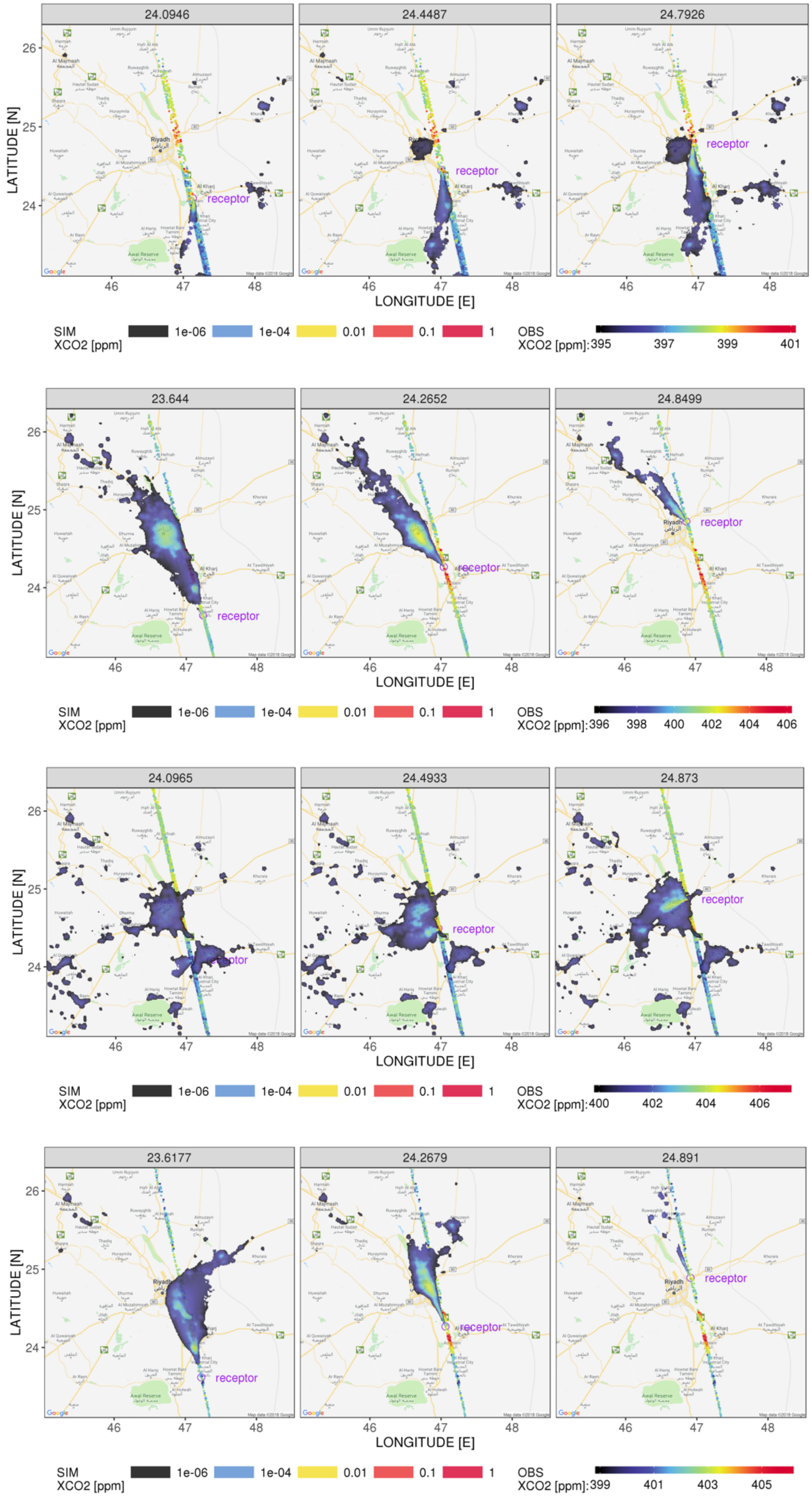

Fig. S10. Same as **Fig. 7e-g**, expect for other overpasses on 20141227, 20151216, 20160115 and 20160216 (from the 1st row to the 4th row).

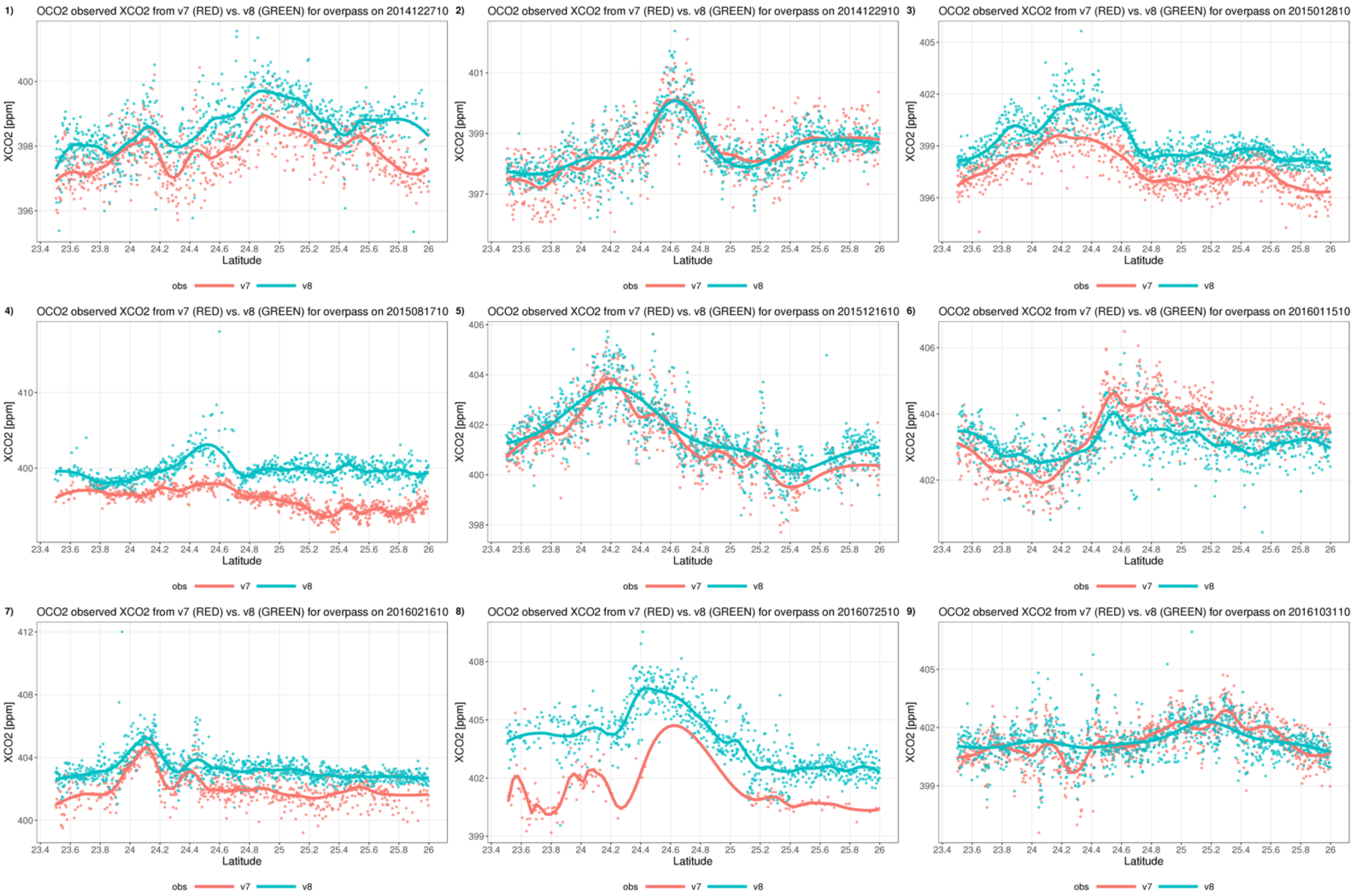

Figure S11. Observed XCO_2 from b7 (red) and b8 (blue) over Riyadh for several overpasses. No data filtering applied in this figure.

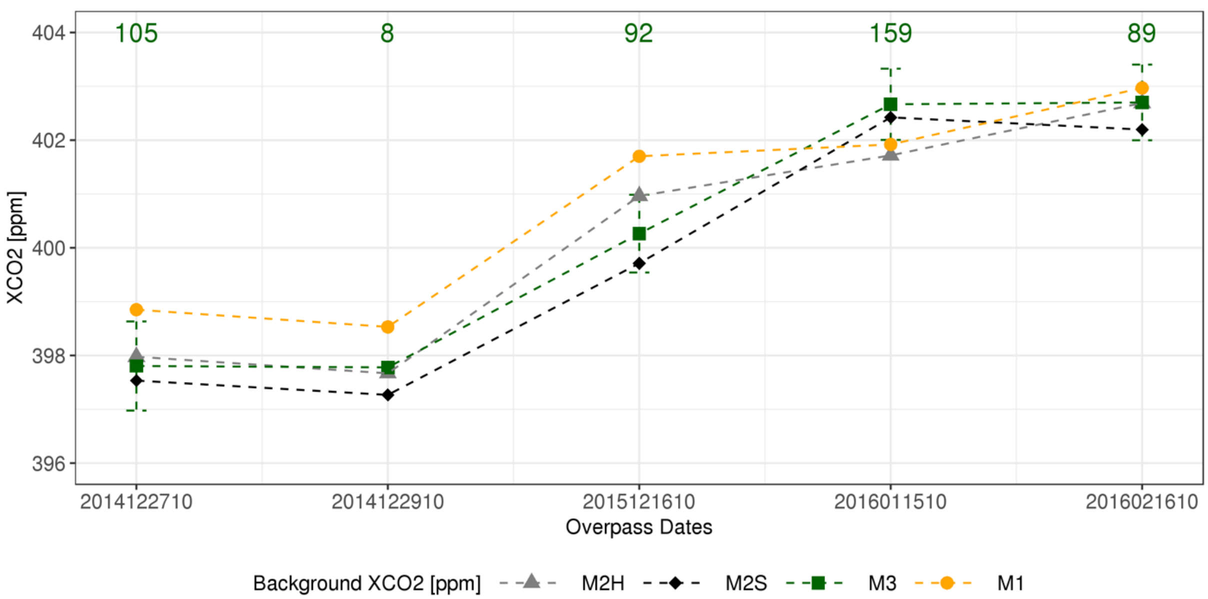

Figure S12. Same as **Fig. 6e**, except for using OCO-2 Lite b8. Numbers labeled in darkgreen donote the amount of screened soundings (QF = 0) using b8 in the background. Due to only 8 soundings for overpass on 2014122910, background uncertainty is hard to estimate (no error bar displayed).

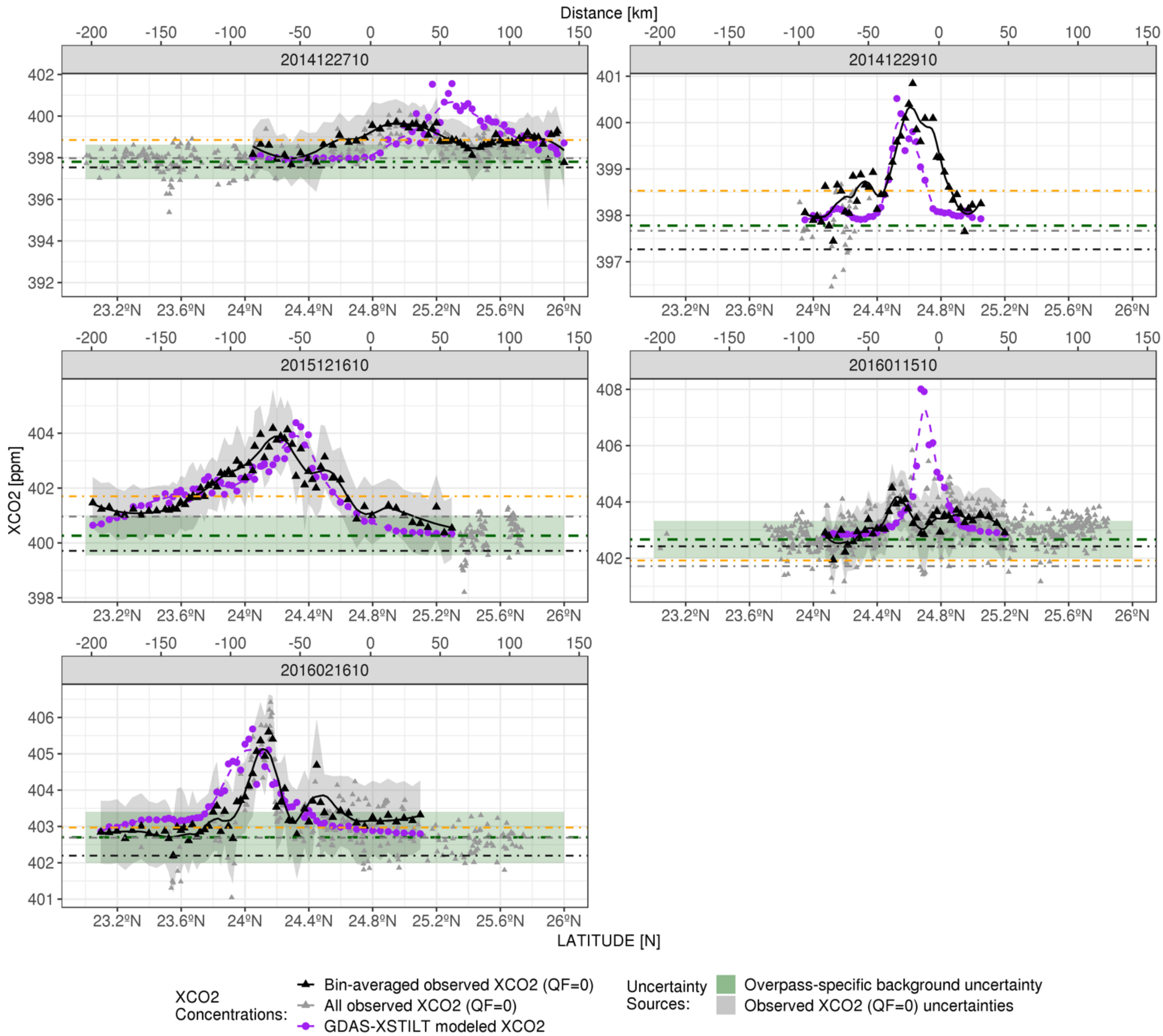

Figure S13. Same as **Fig. S8**, except for using OCO-2 Lite v8, without modeled errors (XCO_2 errors due to atmospheric transport and prior emissions). For the three overpasses on 2014122910, 2015121610, and 2016021610, bin-averaged observations (black solid triangles) are derived based on screened observations using WL = 0 rather than QF = 0, because QF = 0 filtered out almost all observations (gray triangles), making it impossible to calculate latitude-dependent observed enhancements. The intention of choosing these same five overpasses (even though some overpasses have limited screened soundings) is to see the impact of changes in retrieval versions (b7 vs. b8) on modeled and observed enhancements/signals.